Smirnov N.N.[(1)], Nikitin V.F.[(1)], Ivashnyov O.E.[(1)], Maximenko A.[(2)] , Thiercelin M.[(2)]
Vedernikov A. [(3)], Scheid B. [(3)], Legros J.C. [(3)]

Microgravity Investigations of Instability and Mixing Flux in Frontal Displacement of Fluids

The goal of the present study is to investigate analytically, numerically and experimentally the instability of the displacement of viscous fluid by a less viscous one in a two-dimensional channel, and to determine characteristic size of entrapment zones. Experiments on miscible displacement of fluids in Hele-Shaw cells were conducted under microgravity conditions. Extensive direct numerical simulations allowed to investigate the sensitivity of the displacement process to variation of values of the main governing parameters. Validation of the code was performed by comparing the results of model problems simulations with experiments and with the existing solutions published in literature. Taking into account non-linear effects in fluids displacement allowed to explain new experimental results on the pear-shape of fingers and periodical separation of their tip elements from the main body of displacing fluid. Those separated blobs of less viscous fluid move much faster than the mean flow of the displaced viscous fluid. The results of numerical simulations processed based on the dimensions analysis allow to introduce criteria characterizing the quality of displacement. The functional dependence of the dimensionless criteria on the values of governing parameters needs further investigations.

Mail address:
(1) Faculty of Mech. and Math., Moscow M.V.Lomonosov State University, Moscow 119992, Russia
(2) Schlumberger Moscow Research, Hydrokorpus, Leninskie Gory 1-19, Moscow 119992, Russia
(3) Microgravity Research Centre, Free University of Brussels, CP 165/62 Brussels 1050, Belgium

Paper submitted: 05.10.2003
Submission of final revised version: 19.04.2004
Paper accepted: 21.04.2004

1. Introduction

Fundamental results of microgravity investigations serve as a powerful tool, which could help to solve modern problems of terrestrial engineering and technology. Flows in porous media could be much better understood in microgravity studies eliminating the masking effects of gravity.

In frontal displacement of a more dense and viscous fluid by a less dense and viscous one the Rayleigh-Taylor or Saffman-Taylor instability of the interface could bring to formation and growth of "fingers" of gas penetrating the bulk fluid. The growth of fingers and their further coalescence could not be described by the linear analysis. Growth of fingers causes irregularity of the mixing zone. The tangential velocity difference on the interface separating fluids of different density and viscosity could bring to a Kelvin-Helmholtz instability resulting in "diffusion of fingers" partial regularization of the displacement mixing zone. Thus combination of the two effects would govern the flow in the displacement process[1-7].

The problem is relevant to a hydrocarbon recovery, which is performed by the flow of gas under a pressure differential displacing the high viscosity fluid. There are inherent instability and scalability problems associated with viscous fingering that play a key role in the procedure. Entrapment of high viscosity fluid by the low viscosity fluid flow lowers down the quality of a hydrocarbon recovery leaving the most of viscous fluid entrapped thus decreasing the production rate. The gravity effects could play essential role because the problem is scale dependent.

The developed models and obtained results are applicable to description of liquid non-aqueous phase contaminants underground migration, their entrapment in the zones of inhomogeneity, and forecasting the results of remediatory activities in the vicinities of waste storages and contaminated sites.

Another important application of the obtained results is the problem of delivering water to the roots of plants in irrigated

zones. The entrapment of water in porous soils governs the supply of plants' root zones.

2. Experiments on Fluid Displacement in a Hele-Shaw Cell

For experimental modeling of flows in porous media Hele-Shaw cells are used, wherein a small distance between the plates creates enormous drag forces thus simulating the effect of porous media resisting the fluid flow. Fluid flow in a horizontally placed Hele-Shaw cell is usually gravity irrelevant for very thin cells, wherein viscous forces are predominant as related to buoyancy ones. The dimensionless criterion characterizing the ratio of viscous and gravity forces in a Hele-Shaw cell has the following form:

$$\mathrm{Vg} = \frac{\mu u}{\rho g h^2} = \frac{\mathrm{Fr}}{\mathrm{Re}},$$

which is, actually, the ratio of Frude and Reynolds numbers. Here μ is fluid viscosity, u - fluid velocity, $\rho = |\rho_1 - \rho_2|$ - the density difference at the phase interface (if one fluid is air then ρ is equal to the density of the other fluid, g is gravity acceleration, h - cell thickness. For flows in porous media $\mathrm{Vg} \gg 1$. The dimensionless criterion inversely depends on cell thickness in the second power and on gravity acceleration in the first power. Investigating the flow patterns in a Hele-Shaw cell it is necessary sometimes to increase the cell thickness, while determining the correlation between the cell thickness and the width of viscous fingers. To keep the value of Vg criterion at the same level for a set of experiments one needs on increasing cell thikness to reduce essentially gravity acceleration. To have the comparable experimental data one needs to maintain other parameters: viscosity, flow rate - constant. Thus increasing 4 times the cell thickness one needs to perform 16 times gravity reduction, which could be done in parabolic flights.

The microgravity experiments were performed in the frame-

Fig. 1. The Novespace Airbus A-300 Zero-G performing a parabolic flight.

work of the 25th ESA parabolic flight campaign of the Airbus A300 Zero-G (Fig.1) and are shortly described in[13, 14].

The Hele-Shaw cell presented in Fig.2 was built of two plates of 10 mm thick Lexan glass that were 150x200 mm² (a). They were separated by a spacer (b) that is 25 mm wide and closes three sides of the cell. Two spacers of different width were used in order to vary the cell width δ, namely 1.2 and 3.7 mm. Rubber sheets were placed on both sides of the spacer for leak-proofness. All together was fixed with screws (c) spaced every 25 mm along the edges. The injection side was screwed on a slot valve (d) and was proof thanks to an o-ring pressed around the injection slot. This latter was 100 mm large and 4 mm high. The inlet was then planar on the contrary of the outlet that was a 5 mm diameter hole (e) in the bottom of lexan plate. In order to prevent the influence of the outlet geometry on the linear streamlines, cavities (f) were drilled on all the width in the lexan plate, perpendicularly, just before the outlet, as drawn on the bottom plate in Fig. 2.

The injection phase performed under microgravity conditions is shown in Fig. 5. The displacing fluid, namely dyed water, is flowing into the circuit numbered "1". The flow rate is controlled by the rotating pump and ranged from 0.6 ml/s to 18.5 ml/s. The liquid was injected uniformly into the cell by the slot valve. It displaced the steady pre-filling fluid of water-glycerine solution. The punctual outlet was connected to a trash tank.

The characteristic dimensions of the fluid filled domain L x H x δ were: length L = 200mm, width H = 100mm. Thickness δ varied in different experiments. Besides mean flow velocity $U = Q / (H\delta)$ and viscosity ratio $M = \mu_2 / \mu_1$ were also varied in experiments. Table 1 gives the description of 10 experiments, which results are illustrated in Fig. 3 in the form of two successive pictures of the displacement front for times t_1 and t_2 for each experiment. The succession of images in Fig. 3 corresponds to their numbers in the table 1.

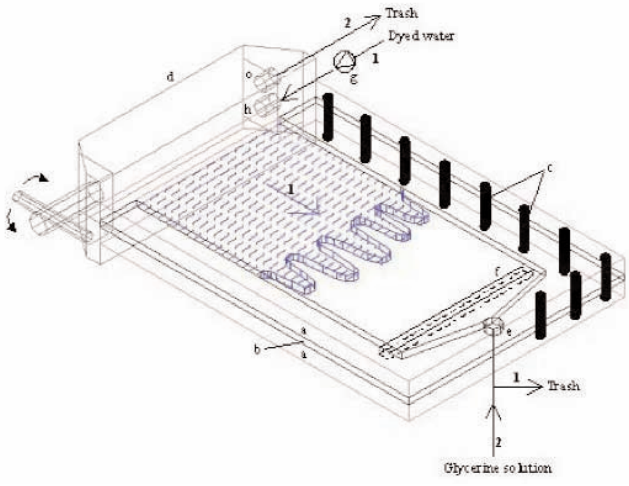

Fig. 2. Experimental cell: (a) Lexan plate - (b) surrounding spacer in Lexan - (c) screw - (d) slot valve - (e) hole - (f) cavity - (g) pump. The circuit "1" is for injection and the "2" is for cleaning/filling

The results of experiments show, that all the parameters under investigation produce an effect on the displacement process. For high viscosity ratio fingers have pear-shaped form with the heads separating and continuing independent motion as blobs of less viscous fluid moving through a more viscous one. Such separated blobs are clearly seen in Fig. 3.3. This is in a good coincidence with our numerical results, which showed that the head of a pear-shaped finger separates and moves independently advancing in a more viscous fluid under the influence of the imposed pressure gradient.

The instability in displacement of a viscous fluid by a less viscous one brings to the formation of a mixing zone.

#	M	U. cm/s	δ, mm	t1, s	t2, s
1	84	5	1.2	0.4	1.6
2	84	2.75	1.2	0.8	3.2
3	84	1	1.2	2	8
4	9	5	1.2	0.4	1.6
5	3	5	1.2	0.4	1.6
6	84	2.75	3.7	0.8	3.2
7	84	1	3.7	2	8
8	9	1	3.7	2	8
9	9	1	1.2	2	8
10	3	2.75	1.2	0.8	3.2

Table 1

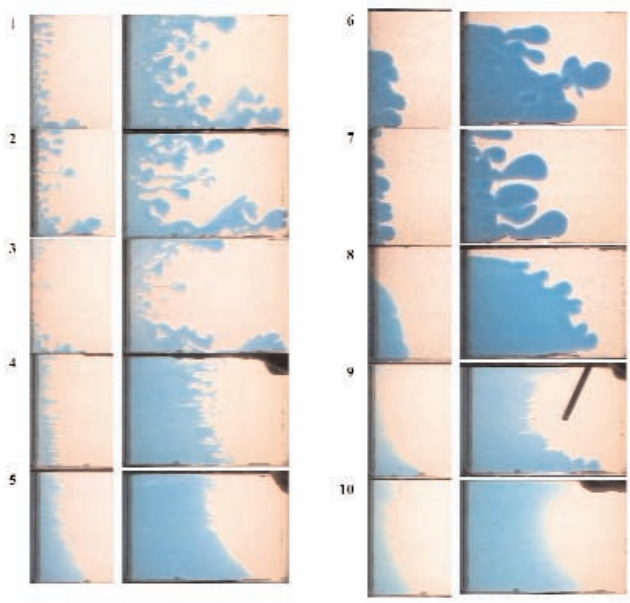

Fig. 3. The succession of flow images for different cases of displacement of a viscous fluid by a less viscous one. The experimental conditions are provided in the table 1.

As it is seen from Fig. 3 the thickness of the fingers λ essentially depends on viscosity ratio $M = \mu_2 / \mu_1$. Fig. 4 illustrates the mean dimensionless thickness of fingers λ / δ as a function of $M^{1/4}$ obtained by averaging the experimental data for different flow velocity U and gap width δ. The results illustrated in Fig. 4 confirm that for the present experimental conditions (high Peclet numbers) all the dependencies are practically linear and have similar inclination. Thus the dependence could be approximated by the following function:

$$\lambda / \delta = 0.35 \, (M^{1/4} - 1).$$

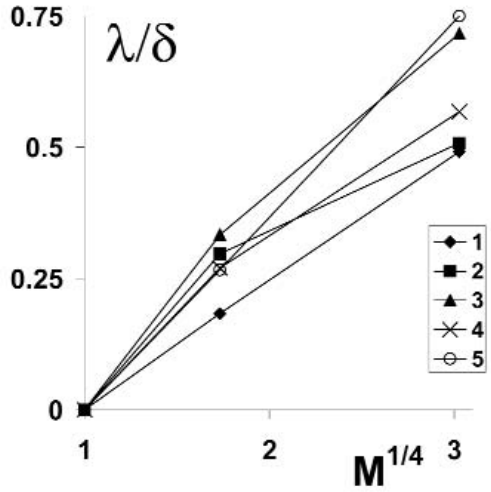

Fig. 4. The mean dimensionless thickness of fingers as a function of viscosity ratio in the power 1/4 for different experiments: Curve 1 - U= 1 cm/s, δ = 1,2 mm; Curve 2 - U= 1 cm/s, δ = 3,7 mm; Curve 3-U= 2.75 cm/s, δ = 1,2 mm; Curve 4 - U= 2.75 cm/s, δ = 3,7 mm; Curve 5 - U= 5 cm/s, δ = 1,2 mm.

Fig.5. Saturation maps for viscous fluids displacement: viscosity ratio M=1, dimensionless time $\tau = t - U / L = 0.219$.

3. Mathematical Model

In the dimensionless form, it is reduced to the following system of equations, boundary and initial conditions:

$$\frac{\partial}{\partial x}\mu(s)\frac{\partial \psi}{\partial x}+\frac{\partial}{\partial y}\mu(s)\frac{\partial \psi}{\partial y}=0, \tag{1}$$

$$u=\frac{\partial \psi}{\partial y}, \qquad v=-\frac{\partial \psi}{\partial x}, \tag{2}$$

$$\frac{\partial s}{\partial t}+\frac{\partial (us)}{\partial x}+\frac{\partial (vs)}{\partial y}=\frac{\partial^2 s}{\partial x^2}+\frac{\partial^2 s}{\partial y^2}, \tag{3}$$

$$\mu(s)=M^{-s}; \tag{4}$$

$$x=0,\ x=\mathrm{A}\cdot \mathrm{Pe}:\ y=\pm\,\mathrm{Pe}/2:\quad \psi=y; \tag{5}$$

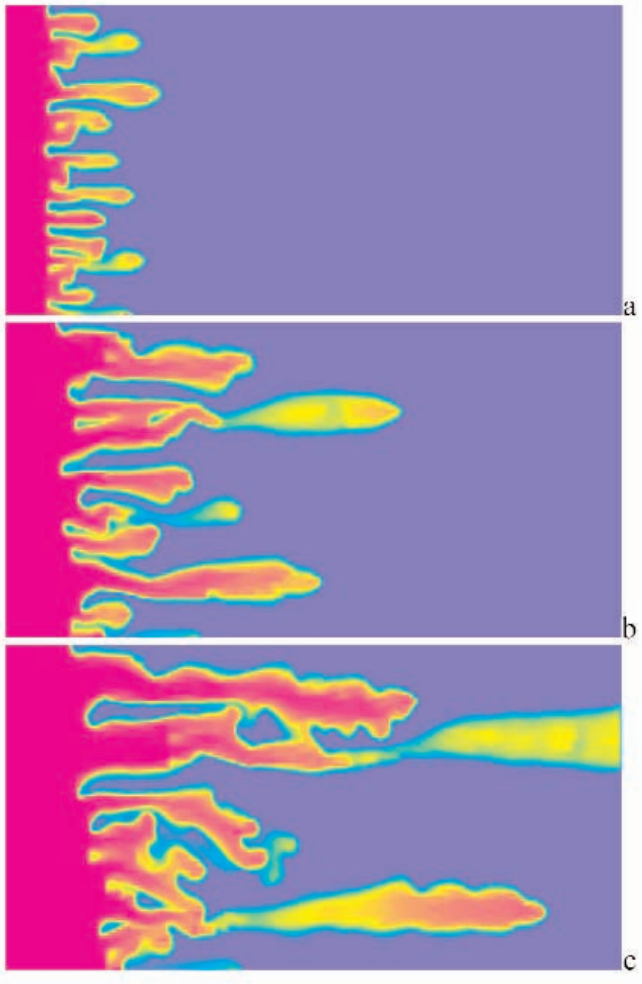

Fig. 6. Saturation maps for viscous fluids displacement: viscosity ratio M=84, dimensionless time $\tau = t - U / L$: a - 0.121; b- 0.248; c- 0.389

$$x=0:\ s=1;\quad x=\mathrm{A}\cdot \mathrm{Pe}:\quad \partial s/\partial x=0; \tag{6}$$

$$y=\pm\mathrm{Pe}/2:\quad \partial s/\partial y=0; \tag{7}$$

$$t=0:\ s=0 \tag{8}$$

The equation (1) is related to distribution of the stream function ψ; it is derived from the Darcy law, the incompressibility and the absence of gravity force conditions. The expressions (2) are related to definition of the stream function. The equation (3) states for the intruding fluid saturation dynamics. The expression (4) determines dimensionless fluid viscosity depending on saturation (more saturation, less viscosity; the type of dependence generalizes harmonic averaging). The boundary conditions (5) state for solidity of lateral walls at $y = \pm\mathrm{Pe}/2$ and regularity of intruding fluid flow at the inlet ($x = 0$) and outlet ($x = A \cdot \mathrm{Pe}$) boundaries. The boundary conditions (6), (7) state for the inflow of the intruding fluid only, free outflow of the mixture, von Neumann's conditions for the saturation affected by diffusion on the lateral walls. The initial condition (8) says that the domain is not filled with the intruding fluid at the first instance. The coordinate system origin is placed in the middle of the inlet section.

The equation (1), expression (2) and boundary conditions (5) were derived from the continuity equation, Darcy law and the non-permeability of lateral walls, correspondingly:

$$\frac{\partial u}{\partial x}+\frac{\partial v}{\partial y}=0, \tag{9}$$

$$u=-\mu^{-1}\frac{\partial p}{\partial x}, \quad v=-\mu^{-1}\frac{\partial p}{\partial y}, \tag{10}$$

$$y=\pm\mathrm{Pe}/2:\quad v=0\ ; \tag{11}$$

The dimensionless parameters in the relationships (1)-(7) are determined as follows:

$$A=\frac{L}{H};\quad M=\frac{\mu_2}{\mu_1};\quad Pe=\frac{Q}{D}=\frac{UH}{D} \tag{12}$$

where L, H are the length and the width of the domain, μ_1, μ_2 are viscosity of intruding and displaced fluids, respectively, Q is the amount of intruding fluid per time unit, U is the average velocity of insertion.

The following scaling factors are used to derive dimensional values from dimensionless ones:

$$\begin{aligned} &\overline{u}=U\cdot u,\quad \overline{v}=U\cdot v,\quad \overline{x}=\frac{D}{U}\cdot x,\\ &\overline{y}=\frac{D}{U}\cdot y,\quad \overline{t}=\frac{D}{U^2}\cdot t,\quad \overline{\psi}=D\psi \end{aligned} \tag{13}$$

Here, values with a bar denote the dimensional parameters rela-

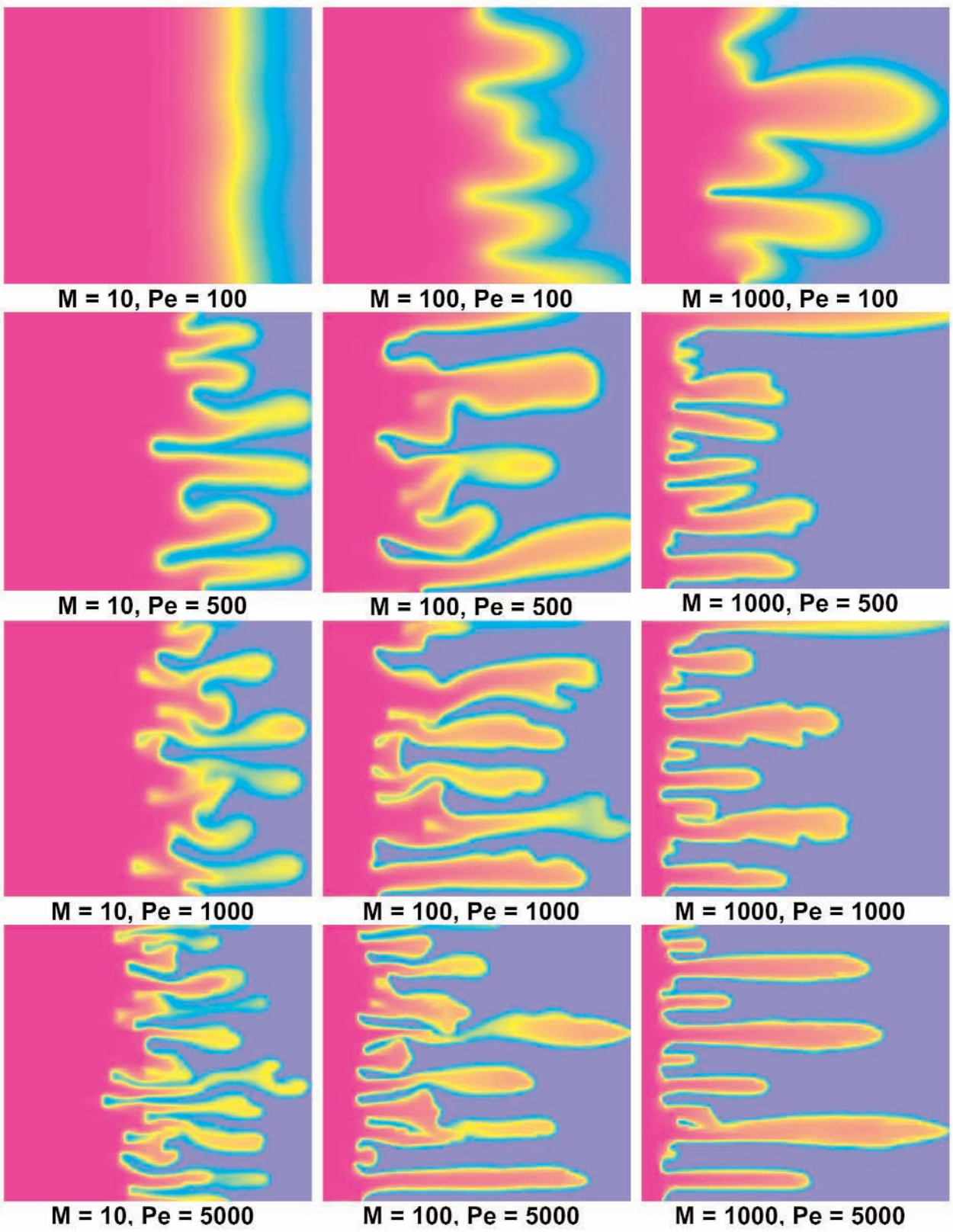

Fig. 7. Different flow patterns in displacement of viscous fluid by a less viscous one from homogeneous media.

ting to dimensionless ones without the bar over them.

Dimensionless viscosity μ is proportional to the dimensional one $\overline{\mu}$ and is scaled upon the viscosity of the fluid being displaced and permeability K of the porous skeleton:

$$\overline{\mu} = \frac{K}{\mu_2} \cdot \mu$$

4. Numerical Modeling

Numerical simulations were performed in a 2-D domain having original size 200 mm x 100 mm, which corresponds to the experimental cell described above. Numerical modeling was performed for the case of a homogeneously permeable medium, which corresponds to a Hele-Shaw cell with flat parallel walls, and for the cases of inhomogeneous permeability as well, which corresponds to the case of obstacle placing in the gap between the two walls in the Hele-Shaw cell. To simulate inhomogeneous permeability 5x5 mm obstacles were used[15], which permeability was assumed two orders of magnitude lower than the one in the rest of the computational domain. The placing of obstacles was 10 or 11 in a row depending on parity. Computational domain grid was 201 x 101 with 5x5 cells obstacles and 5 cells average distance between obstacles edges. Aspect ratio A=2, Peclet number Pe=10000. We used Eulerian approach to solve the problem stated above; the rectangular grid with uniform space steps was involved. Using CFL (Courant - Friedrichs - Levi) criterion we determined the next time step value[9]. Using 2D TVD (2-dimensional total variation diminishing) techniques of the second order[10] we transferred the hyperbolic part of the concentration equation (3) to the next time layer. Using 2D Buleev technique (implicit iterative method for elliptic equations using incomplete factorisation[11] we transfer the parabolic part of the concentration equation (3) to the next time layer.

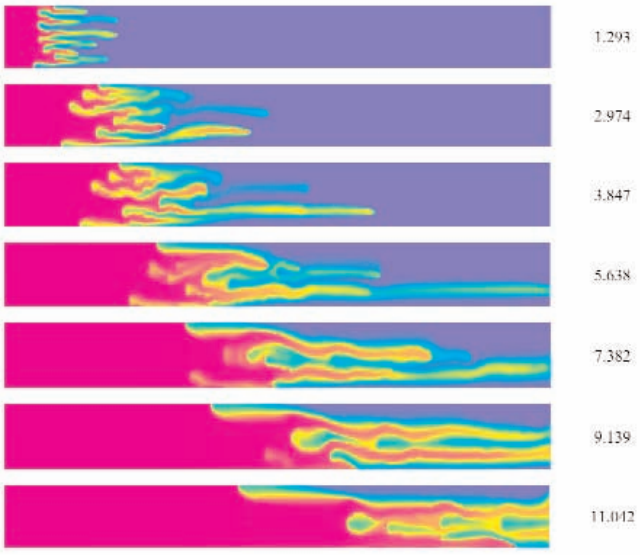

Fig. 8. Saturation of the intrusive fluid for an aspect ratio A=12; viscosity ratio and Peclet number: M = 20, Pe = 1024.

5. Displacement from Homogenous Media

Results of numerical simulations described and analyzed below are relevant to the instability in displacement of miscible fluids, when there is no distinct fluid-fluid interface and fluids could penetrate into each other due to diffusion. Investigating instability in miscible displacement differs greatly from that in immiscible fluids. The presence of a small parameter incorporating surface tension for immiscible fluids allows to determine theoretically the characteristic shape and width of viscous fingers[16, 17], while in miscible fluids theoretical analysis allows to forecast the shape of the tips, but does not allow to determine the width of fingers, which remains a free parameter[18, 19]. Results of extensive numerical simulations of viscous fingering in immiscible displacement[20] have capillary number being one of model parameters, while the present paper deals with miscible fluids displacement characterized by a different set of model parameters incorporating Peclet number.

Numerical modeling of displacement for fluids of equal viscosity was carried out to validate the scheme. The results shown in Fig. 5 testify, that the displacement is stable for the viscosity ratio M=1. Numerical scheme under consideration does not introduce any instability.

As it is known, the increase of viscosity ratio for the displaced and displacing fluids promotes instability in frontal displacement from a homogeneous medium. Fig. 6 illustrates the saturation maps for successive times for the case of high viscosity ratio M=84. To provide a better illustration the characteristic time in displaying results is different from that used in (13), which has a more explicit physical meaning: $\tau = t \cdot U / L = \overline{t} / Pe$.

The results show, that the interface instability arising in viscous fluids displacement (for M >1) brings to formation of fingers of less viscous fluid penetrating the more viscous one. Those fingers grow in time. Some of fingers have the tendency to acquire a peer-shape with the neck getting thinner, and then separate from the displacing fluid. Those separated blobs of less viscous fluid move independently through the more viscous one under the influence of imposed pressure gradient as if floating up in the gravity field. In time mixing of low viscosity fluid with the surrounding one takes place due to diffusion, and the blobs slow down to the velocity of the flow. The traces of the separated blobs, which diffused before, serve as a preferable pathway for new fingers to develop.

Numerical experiments were carried out to investigate the influence of dimensionless governing parameters - Peclet number and viscosity ratio - on the structure of displacement flow and the mixing flux caused by phase interface instability and formation of fingers. The results are shown in the Fig.7, which illustrates characteristic flow patterns obtained for different

values of governing parameters. The aspect ratio was assumed to be equal to A=1.

Fig. 8 illustrates saturation of the intrusive fluid for a higher aspect ratio A=12; *M = 20; Pe = 1024.* It is seen that the small separated blobs of displacing fluid gradually dissolve in the displaced one. Large portions of displaced fluid are being entrapped by the displacing one and move at a much lower velocity than the mean velocity of displacement.

6. Width-Averaged Intrusive Fluid Saturation

The definition of width-averaged saturation of the intrusive fluid was given in our previous report. Using the present notations, it can be written as follows:

$$\langle s \rangle = \frac{1}{Pe} \int_{-Pe/2}^{Pe/2} s(t, x, y)\, dy. \qquad (14)$$

The average saturation $\langle s \rangle$ defined in (14) characterises 1D distribution of the intrusive fluid along the porous domain; many significant values can be expressed in terms of it: the displacement front location and dispersion, the mixing zone length, the amount of displaced fluid trapped in the porous domain behind the displacement front, and so on. This parameter can be easily derived from the solution of 2D problem but our goal is to create a 1D model describing its behaviour without using multidimensional computations. The only way to do this is to set some dynamical model calculating behaviour of a parameter *c(t, x)* depending on some unknown coefficients β_n and then choose the set of β_n influencing *c(t, x)* which minimises a generalised difference between c and $\langle s \rangle$. For example, such a functional can be of the least-squares cost function type:

$$\Phi = \frac{1}{m \cdot A \cdot Pe} \sum_{k=1}^{m} \int_{0}^{A \cdot Pe} \left(c(t_k, x) - \langle s \rangle (t_k, x) \right)^2 dx. \qquad (15)$$

The expression (15) determines the averaged square of difference between derived and modelled width-averaged intrusive fluid saturation. Because of discrete representation of spatially distributed parameters in the numerical model, the integrals in (14)-(15) can be changed by sums, and the final expression for the functional to be minimised will be as follows:

$$\Phi = \frac{1}{m \cdot n_x} \sum_{k=1}^{m} \sum_{i=1}^{n_x} \left(\frac{1}{n_y} \sum_{j=1}^{n_y} s_{ij}(t_k) - c_i(t_k) \right)^2, \qquad (16)$$

Here, t_k (k = 1,..., m) are specified characteristic times, s_{ij} is calculated saturation at $x = x_i$, $y = y_j$, c_i is modelled saturation at $x = x_i$; the least two relating to the same time moments t_k.

The mixing zone length Z can be estimated as follows:

$$Z = x\Big|_{\langle c \rangle = \varepsilon} - x\Big|_{\langle c \rangle = 1-\varepsilon}, \qquad (17)$$

where ε is a small threshold number (e.g. one per cent). It turns that the mixing zone length depends on the value of ε, and we will reference to it as Z_ε.

Figs. 9 a,b illustrate the dependence of the length of the mixing zone Z growth with time. The Fig. 9a relate to Pe = 128, Fig. 9b - to Pe = 1024. The mixing zone grows first proportionally to $t^{1/2}$ (diffusive mode), then proportionally approximately to t (convective mode). The latter proportionality is only approximate one because of the irregular dynamics of fingers, even in a single finger mode when Pe is under critical. The solid lines relate to our simulations, the dotted lines - to those in paper[8], which relate to constant permeability cases. Comparison of the solid and dotted lines in the Fig. 9 shows a good coincidence of integral parameters obtained in our numerical results

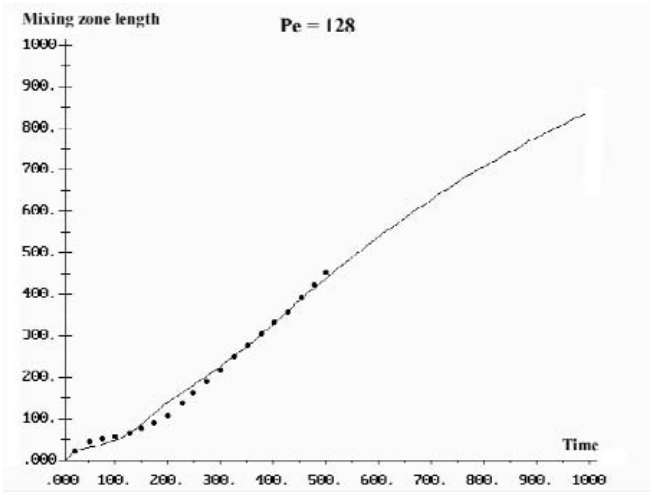

a)

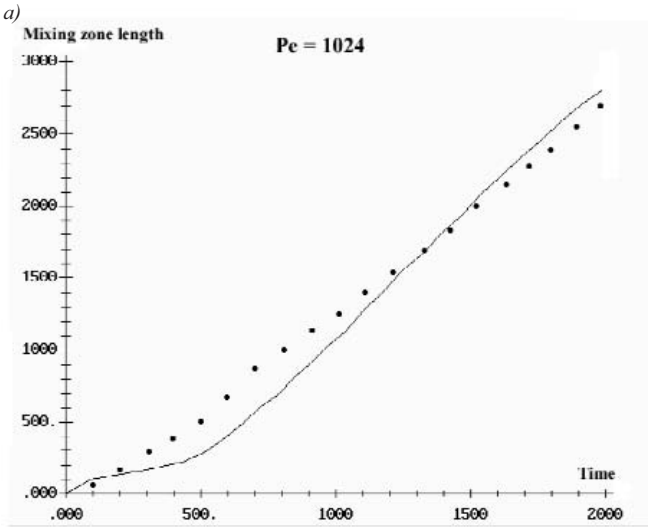

b).

Fig. 9 a. Mixing length vs. time for Pe=128. The dotted line is simulation published in (De Wit & Homsy, 1997). The solid line relates to our simulations

Fig. 9 b. Mixing length vs. time for Pe=1024. The dotted line is simulation published in (De Wit & Homsy, 1997). The solid line relates to our simulations.

with that obtained by other methods. It is seen from Fig. 9 a,b that a good agreement on the mixing zone length is achieved. The difference between the curves obtained in paper[8] and in our simulations can be explained by different factor used to break up the unstable equilibrium and obtain the fingers: slightly disturbed initial conditions in paper[8] and randomly disturbed permeability in the present paper. Moreover, we processed our simulations in the case of small Peclet number to $t = 1000$ and it is seen from Fig. 9a that the convective behaviour of the mixing zone (its length being proportional to time), which established by $t = 500$ gradually changes back for the dispersive one (Z proportional to the square root of time). This comparison serves a good verification for the codes.

Comparison of our results with that obtained in paper[8] shows that for high Peclet numbers similar behaviour of fingers could be noticed: their number decreases in time and only 3 or 4 fingers remain active. On the other hand, contrary to paper[8] in our simulations the results are not symmetrical: fingers laying close to upper and lower boundaries of the domain have better chance to survive. In the long run the finger attached to one of the sides of the domain can finally supersede other fingers.

Reynolds Approach to 1D Averaged Model

Introducing the width averaging operator similar to one applied to s in the expression (14),

$$\langle\varphi\rangle = \frac{1}{Pe}\int_{-Pe/2}^{Pe/2}\varphi dy$$

we derive the behavior of averaged parameters directly from the original multidimensional system of equations. Let us denote a perturbation of a parameter φ with φ'. The perturbation can be defined as difference between actual and averaged values: $\varphi' = \varphi - \langle\varphi\rangle$. Then, by definition we have the following properties:

$$\langle\langle\varphi\rangle\rangle = \langle\varphi\rangle,\ \langle\varphi'\rangle = 0,\ \langle\varphi_1\varphi_2\rangle = \langle\varphi_1\rangle\langle\varphi_2\rangle + \langle\varphi_1'\varphi_2'\rangle,$$

similar to the properties of Reynolds averaging which are being applied to turbulent flows investigation.

Applying the averaging operator to the continuity equation (9) and taking boundary conditions (11) into account, one obtains that the average of horizontal velocity $\langle u\rangle$ is constant along the length of the domain, and it is equal to unit in our method of scaling:

$$\langle u\rangle \equiv 1.$$

Applying the averaging operator to the saturation equation (3) and taking boundary conditions (6), (7) and (11) into account, we get the following equation describing behavior of $\langle s\rangle$:

$$\frac{\partial\langle s\rangle}{\partial t} + \frac{\partial\langle u\rangle\langle s\rangle}{\partial x} = -\frac{\partial\langle u's'\rangle}{\partial x} + \frac{\partial^2\langle s\rangle}{\partial x^2}. \qquad (18)$$

The equation (18) was obtained taking into account non-permeability of lateral walls (eliminating convective flux in the lateral direction) and von Neumann's conditions for saturation on lateral walls (eliminating the second (diffusion) term). Note that the equation (18) is a typical equation for a scalar average value behavior in a turbulent flow: left side terms stand for convection, the first right hand side term is the turbulent mixing (or dispersion) as the opposite to the derivative of the turbulent flux, the second stands for laminar diffusion. The relating theories for turbulent flow then could be taken into account.

The diffusive approach to model the turbulent flux $\langle u's'\rangle$ is based on the Prandtl hypothesis. If we apply it, we get:

$$\langle u's'\rangle = -D_T\frac{\partial\langle s\rangle}{\partial x}, \qquad (19)$$

where D_T is the turbulent diffusion factor which must be modeled itself. Either additional equations or simple algebraic expressions are used to model it in different theories of turbulent mixing. In order to develop such a phenomenology, unknown coefficients regulating some empirical dependence of D_T must be introduced as well. These coefficients could be chosen so as to minimize the difference between the solution derived from multidimensional computations, which model the behavior of the actual parameters (analog of DNS for turbulent flow investigations), and 1D computations modeling the mean values of parameters (analog of a phenomenological theory application).

Using the equality $\langle u\rangle \equiv 1$ for mean velocity and the Prandtl hypothesis (19) for turbulent flux of saturation, and choosing an algebraic expression for turbulent diffusion depending on saturation, we can rearrange the terms in (18) so that it takes the form:

$$\frac{\partial c}{\partial t} + \frac{\partial c}{\partial x} = \frac{\partial}{\partial x}(1 + D_T(c))\frac{\partial c}{\partial x}, \qquad (20)$$

where c denotes the modelled mean intrusive fluid saturation (not to mix with the average of 2D modelling solution denoted with $\langle s\rangle$). The turbulent diffusion depends on the mean saturation itself; the dependence is regulated by unknown parameters $\{\beta_n\}$.

The boundary and initial conditions for the equation (20) matching the correspondent conditions (6), (7) and (8) are the following:

$$x = 0:\ \ c = 1,\ \ x = A\cdot \mathrm{Pe}:\ (\partial c/\partial x) = 0,\ \ t{=}0:\ c{=}0. \qquad (21)$$

In order to get the dependence of mixing coefficient upon c, we should take into account the following considerations. First, that the perturbation increases the flux only in the areas of dispersion, i.e. where s is neither unit, nor zero. Then it is reasonable to assume that the simplest types of $D_T(c)$ should be:

$$D_T(c) = \beta_1 c^{\beta_2}(1 - c)^{\beta_3}. \qquad (22)$$

Second, it could be assumed that the mixing flux is maximal in the zones wherein both phases are present in equal portions, i.e. $c \approx 1/2$. The last assumption leads to the condition

$$\beta_2 = \beta_3.$$

Another approach allowing to model the turbulent flux is following (let us refer it to as the **flux approach**).

Let us abandon the Prandtl's hypothesis now and examine the mixing flux taking into account the properties of the well-developed mixing zone we had obtained in multidimensional computations[14]. To illustrate the necessary features of the mixing zone, there are 3 pictures in Fig. 10a displaying the horizontal velocity, saturation and dimensionless pressure, correspondingly, for a mixing zone calculated for the parameters A =12, Pe = 1024, M =20 at time t = 4.92. This is a typical shape of the mixing zone developed to its full scale in the unstable displacement.

From the Fig. 10a, we can see that the mixing zone is penetrated with several branches - channels filled with liquid of higher saturation (i.e. of lower viscosity). The media surrounding the channels is filled mostly with the fluid of higher viscosity, i.e. the fluid being displaced. Regarding cross sections in the mixing zone, we can derive an ideal picture of it (mostly in the area of low or zero gradient of mean saturation) neglecting the influence of mixing across the width. We can remark that the pure diffusive approach cannot be applied correctly there, because zero gradient of average saturation eliminates the turbulent flux if estimated in accordance with the Prandtl hypothesis.

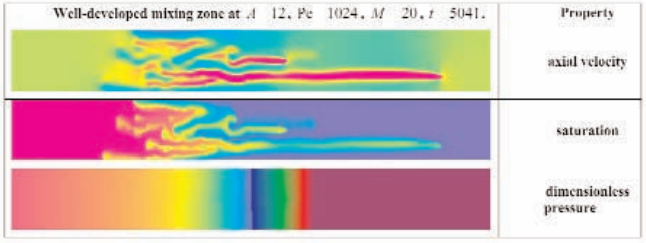

Fig. 10a. Channels in the well-developed mixing zone and other features of the flow.

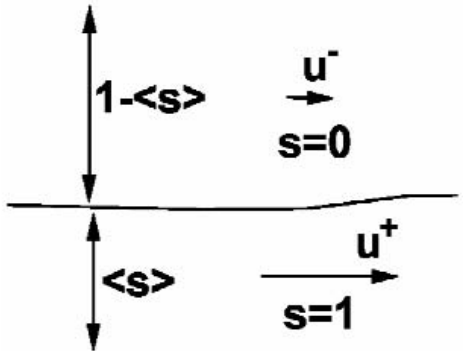

Fig. 10b. Sketch of the mixing zone body (unstable displacement case).

Regarding the sketch shown on the Fig. 10b, we can estimate the velocity and the turbulent flux averages with the following expressions:

$$\langle u\rangle = (1-\langle s\rangle)\, u^- + \langle s\rangle\, u^+ = 1,\ \langle us\rangle = u^+\langle s\rangle,$$
$$\langle u's'\rangle = (u^+ - 1)\langle s\rangle. \qquad (23)$$

Using notation $c = \langle s\rangle$ for 1D modelled width-averaged saturation, we can rewrite (23) as:

$$\langle u\rangle = (1- c)\, u^- + cu^+ = 1,\ \langle us\rangle = c \cdot u^+,$$
$$\langle u's'\rangle = c\,(u^+ - 1). \qquad (24)$$

Let us take the Darcy law (10) into account. The pressure distribution displayed on the Fig. 9 shows that the pressure gradient component along the horizontal (axial) co-ordinate is not disturbed significantly in the cross-section of the flow. This proves that the difference between the lower and the higher velocities is mostly due to the difference in the viscosity of fluids. Assuming $\partial p / \partial x$ to be constant in any cross section of the ideal mixing zone, one could derive the following relationship between the velocities $u^+$and u^-:

$$u^+ = Mu^-,$$

where M is the viscosity ratio. Combining this estimate with (24) one finally obtains the following relationships for the fluxes:

$$\langle us\rangle = \frac{cM}{1+c(M-1)}, \qquad (25)$$

$$\langle u's'\rangle = \frac{c(1-c)(M-1)}{1+c(M-1)}. \qquad (26)$$

The estimate (25) was obtained for an ideal mixing zone body: both fluids were assumed separated (no diffusion in the cross section took place, c was assumed constant along the domain). This estimate is the basis of **the flux approach**: the mixing flux itself depends algebraically on the saturation.

One could notice that the Peclet number does not affect the dependencies (25), (26). The Peclet number can be considered as dimensionless width of the domain; since we did not regard any peculiarities of distribution of the saturation across the mixing zone, then it is evident that the Peclet number would not influence our estimates. In fact, the Peclet number influences the number of fingers mostly, not the stability of the zone itself. Also, when $M \to 1$, the mixing flux (26) tends to zero. If it is lower than 1, the considered structure of the mixing zone does not occur, and the estimate (26) is not valid. Instead, there is a stable displacement without fingering. It means that in (26) the term $(M-1)$ should be replaced with $(M-1)H(M-1)$, where $H(x)$ is the Heavyside function.

Combined approach. Let us examine the drawbacks and advantages of *the flux and the diffusive approaches*. First, one can see that *the diffusive approach* (if single-equation model is considered, of course) can work well only if the gradient of width-averaged saturation is not zero. But the main body of the developed mixing zone has the gradient near zero, and even at zero gradient, the mixing flux may not be zero at all (this was shown in our considerations of *the flux approach*). This drawback could be remedied replacing the diffusive approach by the flux approach, but the last has its own disadvantages.

Let us examine the expression (25), which stands for the total flux. Since this expression is an algebraic one, then the effective velocity of small disturbances propagation (the "sound velocity", or the *flux jacobian eigenvalue*) should be the partial derivative of the expression (25) by c:

$$a = \frac{\partial \langle us \rangle}{\partial c} = \frac{M}{(1 + c(M-1))^2}. \qquad (27)$$

At $c = 1$, $M = 1$, this velocity equals to unit (this correlates with the velocity of displacement equal to unit), but at low c the value of a tends to M. The value of M is not bounded from above, so in case of high viscosity ratio, the velocity of disturbances propagation at the tip of the mixing zone is unrealistically high. This result was obtained as a consequence of the fact that we did not regard the lateral diffusion and some other factors bounding the intrusive channel width in the mixing zone from below. So, the flux approach without improvements is also not an ideal one.

In order to diminish drawbacks of the diffusive and the flux approaches, it is worth to combine them involving scalar weight coefficients. In general, it means that we should model the mixing flux using two empirical dependencies:

$$\langle u's' \rangle = F_T(c) - D_T(c) \frac{\partial c}{\partial x}, \qquad (28)$$

where F_T should be referenced to as mixing convective flux and D_T- as mixing diffusion factor. Both of them depend explicitly on the averaged saturation. In order to model this dependence, rational expression like (26) can be taken for the convective flux, and a polynom - for the diffusion factor. With the expression (28), the original equation (18) modeling averaged saturation behavior is transformed to:

$$\frac{\partial c}{\partial t} + \frac{\partial (c + F_T(c))}{\partial x} = \frac{\partial}{\partial x}(1 + D_T(c)) \frac{\partial c}{\partial x}, \qquad (29)$$

We suggest to use the following expressions for F_T and D_T as a first order approximation:

$$F_T(c) = \alpha \frac{c(1-c)(M-1)}{1 + c(M-1)}, \quad D_T(c) = \beta c^2 (1-c)^2, \qquad (30)$$

The expressions (30) are rather simple, they were obtained using considerations described above. The diffusive coefficient is expressed via a simplified polynomial form as compared with (22). The solution of (29)-(30) with the boundary conditions (21) is unique for a set of unknown coefficients $\{\alpha, \beta\} = \{\beta_k\}$, if the coefficients $\{\alpha, \beta\}$ are set non-negative; however it is not a strict necessity condition.

Computational Techniques for Mixing Flux Modelling

To process 1D calculations, the following algorithm was applied.

1. Input the grid $\{x_i\}$ and time checkpoints $\{t_k\} : 0 < t_1 < ... < t_m$; input *A, M,* Pe.

2. Input $\{\beta_k\}$. Separated from the item 1 because of multiple return possibility.

3. Construct the initial state: $t^0 = 0$, $\{c_i^0\}$.

4. Transition from n-th to (n+1)-th time layer: $\{c_i^n\} \rightarrow \{c_i^{n+1}\}$, $t^{n+1} = t^n + \Delta t$:

   (a) Obtain time step Δt according to modified Courant - Friedrichs - Levy criterion:

   $\Delta t = C \min (\Delta x_i / Q_\delta(a_i))$,

   where $Q_\delta(x)$ is the Harten function depending on the parameter δ regulating artificial viscosity in TVD techniques 1 order step, a is the "sound velocity" - derivative of saturation flux upon saturation. $C < 1$ is a constant (Courant number).

   (b) Process explicitly the convective step, using TVD techniques of the 2nd order.

   (c) Process implicitly the diffusive step using Thomas algorithm to solve 3-diagonal linear equations. The transi tion coefficient is taken from previous iteration.

   (d) Recalculate the transition coefficient and process anot her one iteration (steps b and c) until the number of itera tions is three.

5. Examine the next time checkpoint: if $t^n < t_k \le t^{n+1}$, then interpolate linearly the solutions $\{c_i^n\}$ and $\{c_i^{n+1}\}$ onto the time layer t_k. Save the result into $\{c_{ik}\}$.

6. If the last time checkpoint is passed, then stop. Else, go to the next time layer (item 4).

The process is governed, along with the problem parameters, by the grid distribution, time checkpoints positions, the set of $\{\beta_k\}$, and the following control parameters, which are maintained constant:

$\delta = 0.1$ - artificial viscosity factor used in the Harten function,

$C = 0.2$ - Courant number.

The solution of 1D modelling depends on volatile parameters $\{\beta_k\}$. If obtained, it is easy to construct the functional Φ using the expression (16); the functional should be dependent on the problem parameters, the parameters controlling the numerics, and the volatiles $\{\beta_k\}$. Our goal is to obtain the proper set of volatiles that will minimise the functional under constant value of the other parameters. The "optimal" volatiles will depend on the problem parameters themselves - mostly, the Peclet number and the viscosity ratio.

In fact, we will minimise the following function:

$$\Psi(\beta_k) = \log \Phi \tag{31}$$

The logarithm, instead of the function itself, was chosen for its steep walls surrounding minimum if the last is near zero. Such shape of the function is much better usage for the purposes of its minimisation. Below, we place the description of algorithm used to get a minimum of Ψ along with all the accompanying problems joint together.

In order to minimise the function $\Psi(\beta_k)$ (31) we should apply the standard BFGS technique with the GS (golden section) method for partial 1D minimisation. The algorithm of search for a proper set of unknown coefficients will consist of the following stages.

- The dimensionless parameters A, R, Pe are input together with the parameters controlling 2D problem calculation (calculations stop condition among them). The calculations must be organised providing regular parameters distribution output in different files for different time steps.

- Calculations of 2D problem are processed.

- Among the output of 2D problem, several files relating to different time steps are chosen. The criterion of choice is free; it is preferred that the different files should demonstrate different stages of the displacement process. The choice can be done either manually or automatically according to some criteria.

- The chosen files are processed to obtain the set of time moments t_k and $\overline{c}_{ki} = \langle s \rangle (t = t_k, x = x_i)$. To calculate the last, the following formula is used:

$$\overline{c_{ki}} = \frac{1}{n_y} \sum_{j=1}^{n_y} s_{ij}(t_k). \tag{32}$$

- The initial estimate of β_n set of coefficients is input.

- Using BFGS technique, the function $\Psi(\beta_n)$ is minimised. In order to calculate Ψ for a given set of parameters, the following method is used.

  - Calculate 1D problem for a given $\{\beta_n\}$ and obtain solution for the time moments as closer to t_k as possible. In order to simplify computations, the grid should match the grid of the 2D problem, and the checkpoints should match the times chosen from the saved 2D solution times.

  - Calculate Φ using $c(t_k)$ and $\overline{c}_{ki}$, then tale a natural logarithm of it.

The standard BFGS method used in our algorithm is the following. It consists of an iteration process where each iteration is used to diminish the goal function gradually. The initial estimate of parameters is input before processing iterations. Then, the following order of actions is processed on each iteration.

- Calculate the function and its gradient: $\Psi(\beta)$, $\Gamma = \partial\Psi / \partial\beta$. If it is not a first iteration, then save old gradient into Γ_0 before calculating the new one, and after calculating the new gradient, get the difference: $\gamma = \Gamma - \Gamma_0$.

- If it is a first iteration, or conditions to reset the Hess matrix are taking place, then the Hess matrix (actually, approximation of the inverse to the Hessian in the extreme point) is initiated with a unit matrix: $H = U$. In the other case, the Hess matrix is evaluated using the following formula:

$$H^+ = H - \left(1 + \frac{\gamma \cdot H\delta}{\gamma \cdot \delta}\right)\frac{\delta \times \delta}{\gamma \cdot \delta} + \frac{(\delta \times \gamma)H + H(\gamma \times \delta)}{\gamma \cdot \delta}, \tag{33}$$

where the dot denotes scalar product, the cross denotes the diadic product, and no sign denotes matrix product (matrix by matrix resulting in matrix or matrix by vector resulting in vector); δ is the vector of difference between two estimates, see below.

- The direction of search is evaluated: $d = -H\Gamma$ (34)

This function can be normalised in order to simplify further partial 1D minimisation.

- The function $f(\lambda)$ depending on a scalar parameter λ is minimised using 1D minimisation algorithm. After that λ_0 is obtained minimising f which is the following:

$$f(\lambda) = \Psi(\beta + \lambda d). \tag{35}$$

We can remark that the initial estimate of λ should be taken as zero. Actually, we will use the GS algorithm with premature bounding of the extreme; it is described below.

- Save the old estimate: $\beta_0 = \beta$, evaluate the new one: $\beta = \beta_0 + \lambda_0 d$, and get the difference: $\delta = \beta - \beta_0$. This difference is used in evaluating the Hess matrix using (32)

• Check the criterion of iterations break (one can use δ and the tolerances set input beforehand). Also, one can check the following: if λ_0 is negative, then it is time to reset the Hess matrix into unit on the next iteration. If the iteration process is not to be broken, go to next iteration.

We can remark that each of the iterations of the BFGS method requires N +1 evaluations of the functional Ψ where N is the number of parameters β_n (not including the number of iterations on 1D minimisation stage). Those evaluations require solution of 1D problem from $t = 0$ to $t = t_m$, therefore it is the most time consuming part of the process.

The algorithm of 1D minimisation using golden section techniques for bounded extreme and bounding technique before applying GS, being applied to a function $f(\lambda)$ with initial estimate equal to zero and initial value of function $f_0 = f(0)$ regarded as known, can be described as follows.

• Bounding stage.

  • Input initial Δ (argument increment), $\lambda^- = -\Delta$, $\lambda^+ = \Delta$,

  • Evaluate $f^- = f(\lambda^-)$, $f^+ = f(\lambda^+)$.

  • If $f^- > f_0$ and $f^+ > f_0$ then the extreme is bounded within the segment $[\lambda^-, \lambda^+]$; no other processing on the bounding stage is needed. Else, determine the direction of search (positive if $f^+ < f_0$; negative if $f^- < f_0$; if both are lower, then the direction points to the lowest of them).

  • In case of the negative direction, exchange $\lambda^+ \leftrightarrow \lambda^-$, $f^+ \leftrightarrow f^-$ and alter the sign of Δ.

  • Process the cycle of bounding. On each iteration:

    • Store successively: $\lambda^- = \lambda_0$, $\lambda_0 = \lambda^+$; $f^- = f_0$, $f_0 = f^+$.

  Evaluate $\lambda^+ = \lambda_0 + \Delta$, $f^+ = f(\lambda^+)$.

  • If $f^+ > f_0$, then the extreme is bounded between λ^- and λ^+. Otherwise, increase $\Delta \leftarrow 2\Delta$ and repeat the cycle. Note: the cycle will finish only if the function has a real minimum not in the infinity. To stop infinite cycling one can break the cycle either after a definite number of iterations or after exceeding a definite absolute value of λ^+.

• After processing the bounding algorithm, the bounds λ^- and λ^+ are not necessarily ordered first lower second higher. The following GS algorithm does not require this order.

• Golden section minimisation algorithm. On input, we have λ^- and λ^+ bounding the extreme point. Then, the following cycle is processed while $|\lambda^+ - \lambda^-|$ exceeds some given tolerance.

• Evaluate $a = g_1\lambda^- + g_2\lambda^+$, $b = g_1\lambda^+ + g_2\lambda^-$, where $g_1 = 0.618$, $g_2 = 0.382$ (golden section proportions). Then, evaluate $f_a = f(a)$, $f_b = f(b)$.

• If $f_a > f_b$, then set $\lambda^- = a$. Otherwise, set $\lambda^+ = b$.

• Repeat the cycle, if the difference exceeds tolerance. Otherwise, return either a or b depending on the result of previous comparison. One should not return an average because it is not guaranteed with sure that function of it is less than the evaluated one.

The 1D-minimisation stage requires $2 + n_b$ evaluations of function on the bounding stage and $2n_s$ evaluations on the GS stage; n_b, n_s are numbers of iterations at each stage, correspondingly. To reduce the job, a proper value of initial increment Δ must be set: too low brings to high number of iterations on the bounding stage, too high increases iterations number on the GS stage. The value of tolerance affects the GS stage number of iterations only: it is proportional to logarithm of the tolerance.

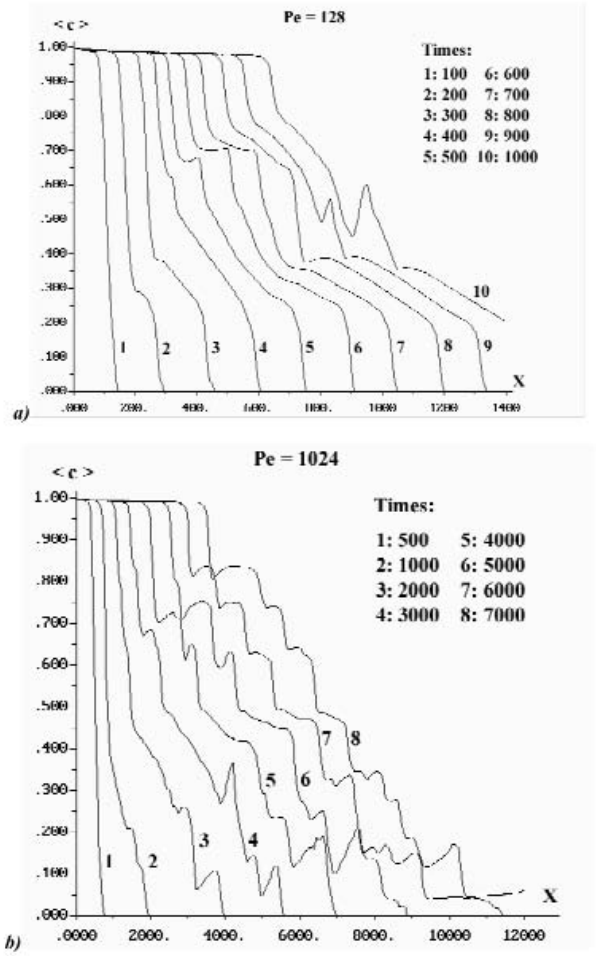

Fig. 11. Averaged by width concentration profiles for successive times: a - Pe=128, M=3; b - Pe=1024, R=3.

Results of Multidimensional Modeling Processing Aimed at Developing Mixing Flux Coefficients

The technique described above was applied to search for proper coefficients of the turbulent flux and the turbulent diffusion coefficient (30). At first, we obtained the following results for $\alpha \equiv 0$ (diffusive approach case).

The Figs. 11a, b illustrate the behaviour of concentration averaged across the width of the domain. In spite of disturbances caused by arbitrary fingering, it develops regularly enough to have a chance to be described by the developed techniques. One can see that the behaviour of the averaged concentration is much more regular and therefore predictable in case of sub-critical Peclet number (Fig. 11a). The Fig. 11a relates to *Pe =128, M = 20*, Fig. 11b - to *Pe = 1024*, *M = 20*. The behaviour of averaged concentration for supercritical Peclet number is much more irregular: non-monotonous disturbances rise up from t=2000 (curve 3) and develop further.

The table beside contains the diffusion coefficient obtained for different *M* and *Pe*, and the fit quality (contrary to Ψ function, which decreases on increasing the fit quality, the present parameter grows higher the better the fit is).

Each entry in the Table 2 relating to one pair of *Pe, M* consists of two numbers: the coefficient itself placed above and the corresponding fit quality below.

Together with the main tendency of rising β with Pe and *M*, the table 2 shows some anomaly results. The first anomaly is situated in the right lower corner, it shows a very good qualities of fit (orders of magnitude higher as being compared to the other entries) but almost zero value of the coefficient. It means that under those conditions, the regular displacement took place almost without motion in lateral directions. In this case, the width-averaged saturation coincides with the saturation itself. The second is higher coefficient at Pe = 256, *M* = 3 than at Pe = 512, *M* = 3, contradictory to the main tendency. However, the quality of fit is good in both cases. Maybe, it could be explained by some unresolved tendency of the coefficient behaviour near the critical curve separating zones of regular and irregular displacement.

Diffusion coefficient and fit quality. Diffusive approach case

Pe	*Viscosity ratio M*			
	20.09	**7.39**	**4.48**	**3.00**
1024	4787 *5.50*	2461 *5.76*	1920 *6.33*	1067 *6.65*
512	2058 *5.46*	1472 *5.62*	728.0 *5.61*	320.2 *5.92*
256	985.4 *4.93*	727.4 *4.86*	446.1 *5.28*	420.1 *6.95*
128	489.5 *5.20*	165.9 *5.24*	86.11 *5.89*	0.22 *12.94*

Table 2. Diffusive approach case. Coefficient β and the fit quality

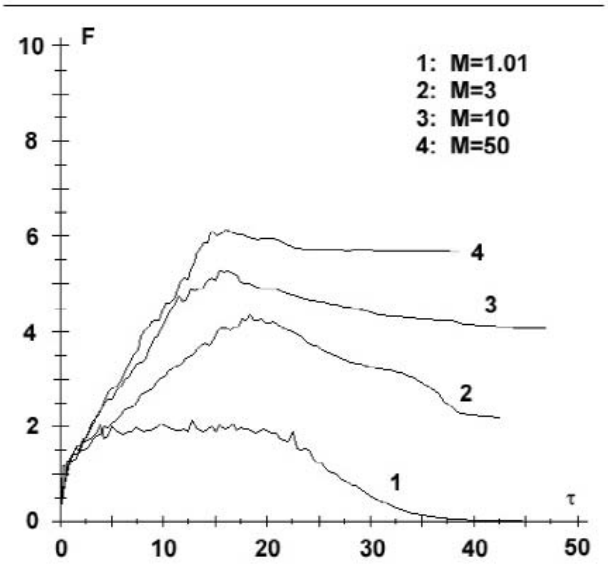

Fig. 12. Evolution of the fingering index with time for different viscosity ratios.

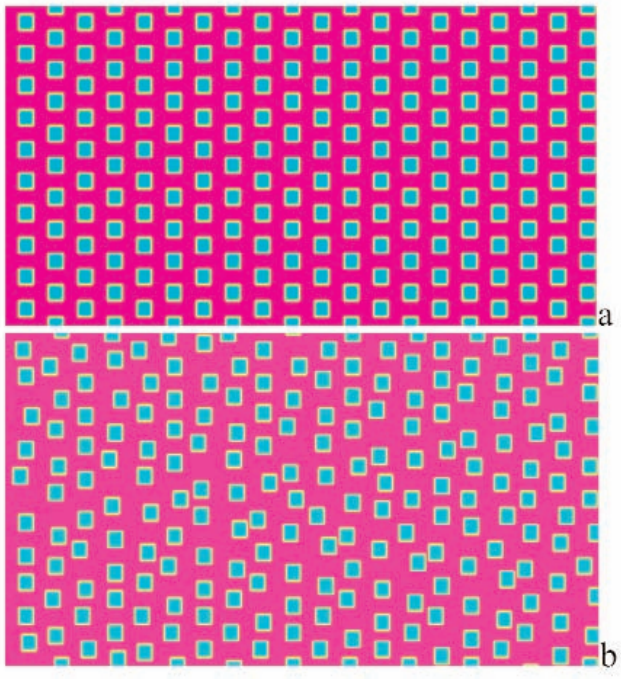

Fig. 13. Regular (a) and randomized (b) obstacles placing in the computational domain.

8. Integral Characteristcs of Displacement Process

The following integral dimensionless parameters are to be traced with time to provide the characteristics for the displacement procedure[12] .

Displacement Quality
The amount of fluid 2 remaining in the domain characterises the quality of displacement. It is calculated as:

$$B = \int (1 - c) dV, \tag{36}$$

where the integral scopes the whole domain. The initial amount is equal to the dimensionless volume in the domain.

Fingering index
This is a special parameter proportional to ratio of the dimensionless interface surface within the domain to the volume of the domain. The increase of interface instability leads to the increase of this index. The magnitude of it will be referenced to as *F*.

In order to compute the fingering index, a rectangular grid is required in the domain. Then, if the parameter $c = \alpha_{ij}$ is determined in the nodes of the grid, the fingering index is calculated as follows:

$$F = \frac{1}{n_y} \sum_{j=1}^{n_y} \sum_{i=1}^{n_x - 1} \left| \alpha_{i+1,j} - \alpha_{i,j} \right| + \frac{1}{n_x} \sum_{i=1}^{n_x} \sum_{j=1}^{n_y - 1} \left| \alpha_{i,j+1} - \alpha_{i,j} \right|, \tag{37}$$

where n_i, n_j are numbers of grid nodes in horizontal and vertical directions. The description of the fingering index above looks like slightly modified definition of the total variation of α by Yee, Warming and Harten (1985)[10]. Plots of the fingering index changing with time for different values of are shown on the fig. 12. To obtain results on mixing induced purely by instability diffusive mixing was assumed to be zero for the present run (infinite Peclet number)[12]. The curves obtained have similar properties: first the curves rise up to maximal values then slightly decrease. It can be seen from the Fig. 12 that the increase of the viscosity ratio *M* increases the fingering index.

9. Displacement from Inhomogenous Media

To simulate inhomogeneous permeability 5x5 mm obstacles were used, which permeability was assumed two orders of magnitude lower. The obstacles placing is shown in Fig. 13. Both regular and randomized sets of obstacles within a Hele-Shaw cell were investigated. In all the runs of numerical simulations the same pattern of randomized obstacles was used.

Numerical simulations of a viscous fluid displacement by a viscous fluid of the same viscosity (*M=1*) from the saturated inhomogeneous medium showed, that contrary to displacement from a homogeneous medium (Fig. 5) the dispersion and mixing of fluids is much stronger. The fluid concentration maps

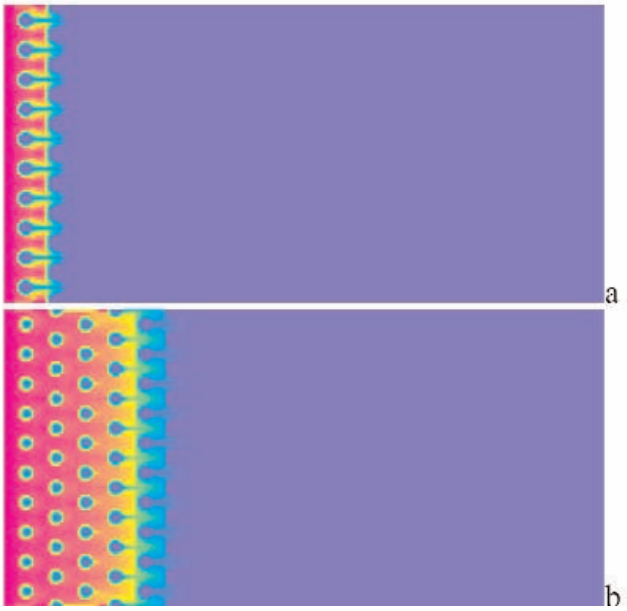

Fig. 14. Saturation maps for viscous fluids displacement: viscosity ratio M=1, dimensionless time $\tau = t - U / L$: a- 0.053; b- 0.181.

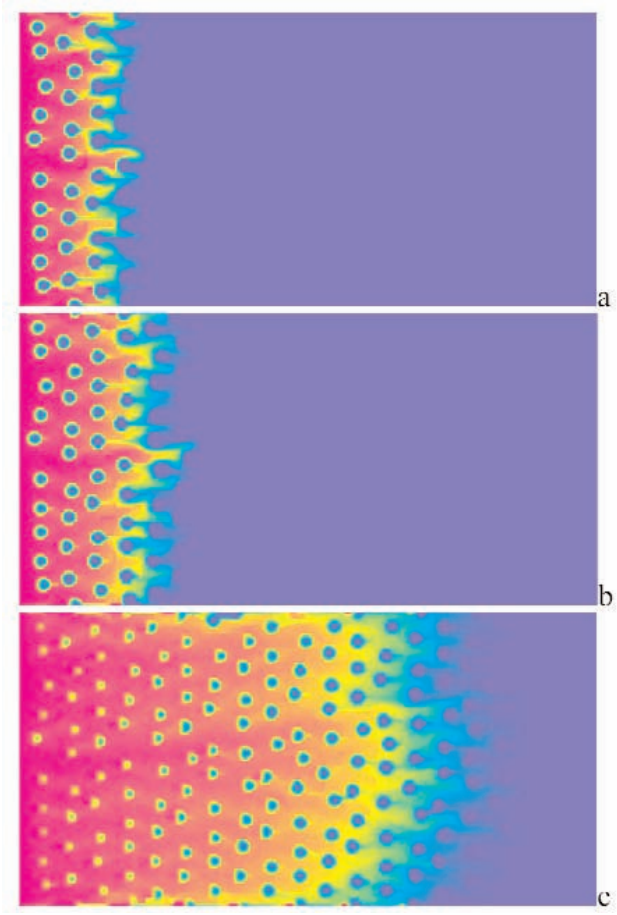

Fig. 15. Saturation maps for viscous fluids displacement: viscosity ratio M=1, dimensionless time $\tau = t - U / L$: a- 0.117; b- 0.167; c- 0.504.

for displacement from inhomogeneous samples with regular obstacles placing are shown in Fig. 14. As it is seen from the Fig. 14 the flow branching effect due to inhomogenity of permeability brings to a much stronger dispersion of fluids and to a sharp increase of the mixing zone.

Irregularity in obstacles placing increases the dispersion even more for the present numerical experiment (Fig. 15).

Based on the results of numerical simulations described above one could come to the conclusion that regular and irregular inhomogenity of permeability both promote flow instability and formation of a mixing zone due to fluids dispersion. This conclusion is valid for fluids of low viscosity ratio (practically equal viscosity).

As it was shown (Figs. 6 and 7), the increase of viscosity ratio of the displaced fluid to the displacing one promoted interface instability and viscous fingering in frontal displacement from a homogeneous medium. Fig. 6 illustrates the saturation maps for successive times for the case of high viscosity ratio *M=84*. Contrary to the previous numerical experiment the results of simulations for the same fluids displacement from a medium of inhomogeneous permeability ("obstacles" of two orders lower permeability) show that regular obstacles inhibit instability and shorten the length of the mixing zone (Fig. 16). The randomization of obstacles brings to an increase of the mixing zone (Fig. 17) as compared with the regular obstacles. The percolation of fluid along the widest zones of low permeability takes place mostly.

The above results show that the presence of inhomogenity in porous medium could promote instability of displacement for low viscosity ratio, and, on the contrary, could inhibit dispersion and mixing for high viscosity ratio.

The opposite role of obstacles for displacement of fluids characterised by different viscosity ratio is likely to be due to the dependence of the characteristic size of fingers on viscosity ratio. As it is shown by experiments illustrated in Fig. 4 and by numerical simulations illustrated in Fig. 7, the average width of a finger grows on increasing viscosity ratio. Both the increase of viscosity ratio and introducing inhomogeneous permeability promotes instability in frontal displacement. However, introducing obstacles we, at the same time, introduce another characteristic size: obstacles spacing. Until the characteristic size of fingers remains smaller than the obstacle spacing both effects contribute to promoting instability. On increasing viscosity ratio one comes to a situation, under which the characteristic size of disturbance (finger thickness) in its growth surpasses the obsta-

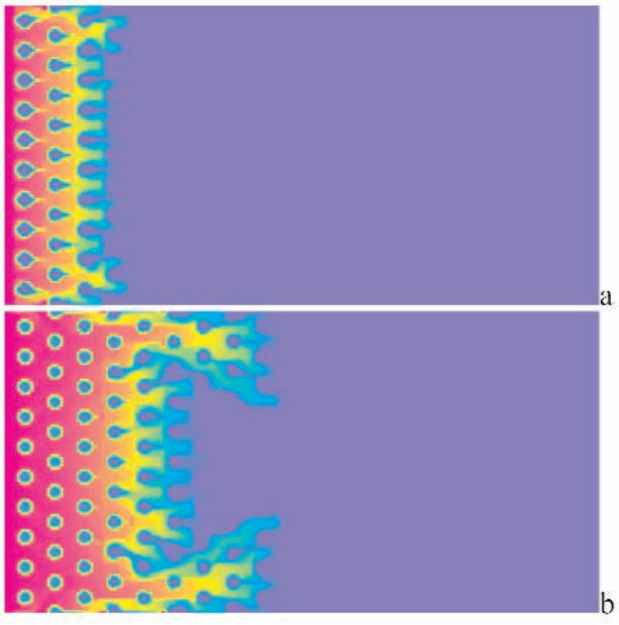

Fig. 16. Saturation maps for viscous fluids displacement: viscosity ratio M=84, regular obstacles, dimensionless time $\tau = t \cdot U / L$*: a- 0.097; b- 0.218.*

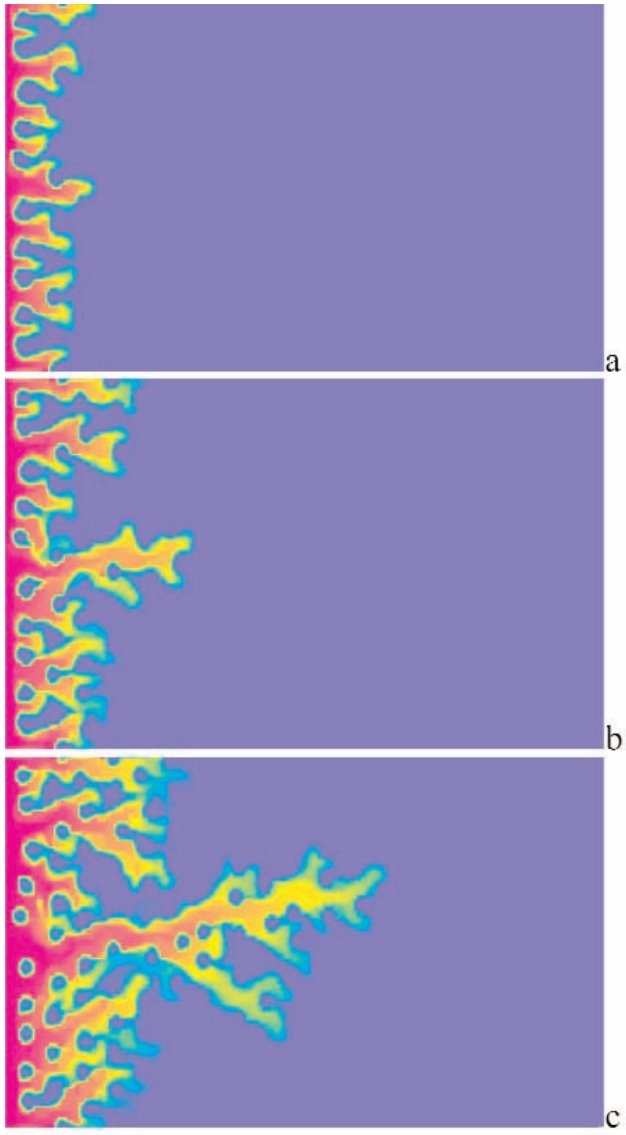

Fig. 17. Saturation maps for viscous fluids displacement: viscosity ratio M=84, random obstacles, dimensionless time $\tau = t \cdot U / L$*: a- 0.053; b- 0.089; c- 0.166.*

cle spacing. Then due to geometrical constraints displacement from each gap between neighbouring obstacles should be stable, because the disturbances, which could grow, surpass the gap width. However, randomisation of obstacles, brings to formation of gaps of different width. That creates preferable pathways for fluids displacement thus promoting instability.

Experimental investigations of the role of inhomogenity was performed on a similar hardware, but the Hele-Shaw cell itself contained additional obstacles (Fig. 18). The modified Hele-Shaw cell with obstacles provides much better conditions for modelling dispersion in a porous medium than the classical Hele-Shaw cell. The classical cell without obstacles simulates drag forces in pore flow, while the cell with obstacles enables to simulate pore branching as well that is crucial for determining the mixing flux.

The colour added to the displacing fluid enables to trace the mixing zone evolution thus providing the data for determining the mixing coefficient.

The characteristics sizes of the cell: length $L = 200\ mm$, width $B = 100\ mm$, thickness $h = 3.7mm$, the size of obstacles *5mm x 5mm x 3.7mm*. The displacing fluid is delivered from the right hand side. The sink for the displaced fluid is in the left hand side of the cell. The fluids are water and water-glycerin solutions that makes it possible to vary the viscosity ratio in a wide range.

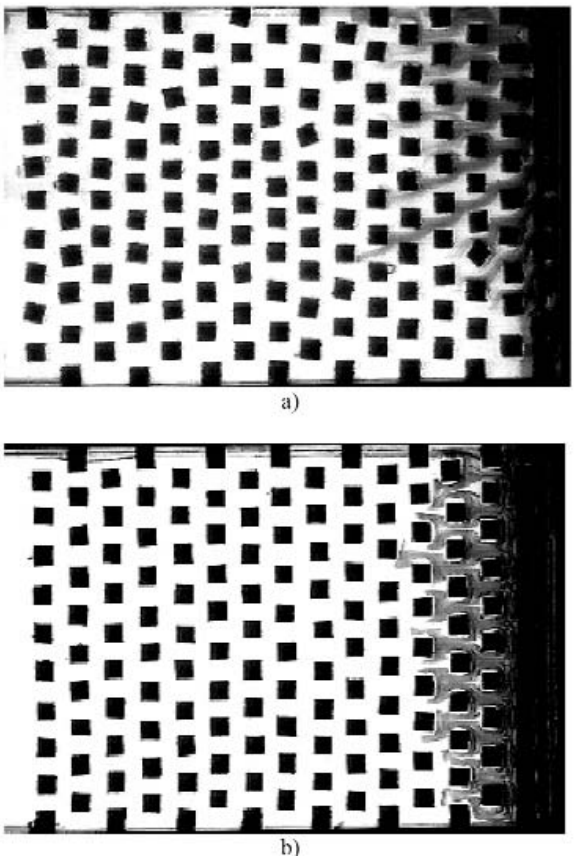

Fig. 18. Flow images for different cases of displacement of a viscous fluid by a less viscous one from a modified Hele-Shaw cell with obstacles. The displacement velocity U = 5 cm/s, time 0.60 s. The viscosity ratio: a - M= 3, b - M = 84.

Fig. 18 a, b illustrates the experiment on displacement of a highly viscous fluid by a less viscous one from a modified Hele-Shaw cell with obstacles. The flow rate corresponds to a mean displacement velocity $U = 5cm/s$. Both figures correspond to time 0.60 s after the beginning of displacement process. The viscosity ratio was equal to $M = 3$ in Fig. 18a, and it was $M = 84$ in Fig. 18b. It is seen that for the present experiment the size of the mixing zone is larger for the case of lower viscosity ratio.

Investigations of peculiarities of instability in fluids displacement from inhomogeneous porous media should be continued. The effect of placing obstacles on stabilization of displacement for high viscosity ratios was also observed in experiments described in the paper[15], but now the undertaken theoretical investigations allowed to suggest the explanation for this effect.

10. Conclusions

- Displacement of viscous fluid saturating permeable media by a less viscous one was investigated experimentally and simulated numerically for miscible fluids.
- Comparison of experimental results with that of numerical modeling demonstrated a good coincidence and testified the adequacy of the developed mathematical model.
- Experimental and numerical investigations showed that some fingers had the tendency to acquire a peer-shape with the neck getting thinner, and then separate from the displacing fluid.
- Experimental and numerical investigations showed that the thickness of "viscous fingers" increases with the increase of viscosity ratio.
- The effect of Hele-Shaw cell thickness on viscous fingering in displacement of miscible fluids was investigated experimentally. Processing of experimental results allowed to develop for high Peclet numbers a universal dependency of mean dimensionless thickness of fingers on viscosity ratio.
- First experiments in a modified Hele-Shaw cell with obstacles were conducted and analyzed.
- In displacement of a viscous fluid by a less viscous one originating fingers can both split and agglomerate. It was shown that for the regarded values of parameters the tendency to agglomerate was predominant and the number of fingers was decreasing until it reached some stable value.
- A universal model was developed, which allows to determine the mixing zone and the averaged mixing flux based on the results of multi-dimensional modeling. The developed model allows to provide quantitative evaluations for the displacement quality and mixing induced by the instability in frontal displacement of fluids from

homogeneous media.

- Experiments show that in a traditional Hele-Shaw cell the increase of viscosity ratio and Peclet number increases instability, while in a cell with obstacles the dependency on viscosity ratio could be quite the opposite.
- The presence of inhomogenity in porous medium destabilises regular displacement, while it could stabilise an irregular one under definite conditions.
- Innhomogenity of a definite regularity could stabilise the displacement of a highly viscous fluid by a less viscous one.

11. Acknowledgements

The authors wish to acknowledge the generous support of INTAS (Grant Aral 00-1075) NATO Scientific and environmental affairs division (Grant EST.CLG.979157), SSTC Program of Belgium. The authors wish to thank Schlumberger for permission to publish the paper. The authors are grateful to ESA and Novespace for the valuable help in performing experiments under the reduced gravity conditions in parabolic flights of the Airbus A300 Zero-G.

12. References

[1] *Barenblatt G.I., Entov V.M., Ryzhik V.M.* Theory of fluids flows through natural rocks. Kluwer Academic Publishes - Dordrecht / Boston / London, 1990.

[2] *Nield D.A., Bejan A.* Convection in porous media. Springer-Verlag - New York / Berlin / Heidelberg / London, 1992.

[3] *Bear J., Bachmat Y.* Introduction to modelling of transport phenomena in porous media. Kluwer Academic Publishes - Dordrecht / Boston / London, 1990.

[4] *Kaviany M.* Principles of heat transfer in porous media. Dover Publications Inc. - New York, 1988.

[5] *Smirnov N.N., Dushin V.R., Legros J.C., Istasse E., Bosseret N., Mincke J.C., Goodman S.* Multiphase flow in porous media - mathematical model and micro-gravity experiments. Microgravity Science and Technology, IX(3), 1996, pp. 222-231.

[6] *Smirnov N.N., Legros J.C., Nikitin V.F., Istasse E., Norkin A.V., Shevtsova V.M., Kudryavtseva O.V.* Capillary driven filtration in porous media. Microgravity Science and Technology, Hanser Publ., 1999, XII, pp. 23-35.

[7] *Smirnov N.N., Nikitin V.F., Norkin A.V., Kiselev A.B., Legros J.C., Istasse E.* Microgravity investigation of capillary forces in porous media. Space Forum 2000, 6(1-4), pp. 1-10.

[8] *De Wit A., Homsy G.M.* Viscous fingering in periodically heterogeneous porous media. Part II. Numerical simulations. J. Chem. Phys. 1997. Vol. 107(22), 9619.

[9] *Anderson D.A., Tannenhill J.C., Pletcher R.H.* Computational fluid mechanics and heat transfer. New York, McGraw-Hill, 1984.

[10] *Yee H.C., Warming R.F., Harten A.* Implicit total variation diminishing (TVD) schemes for steady-state calculations. Journal of Computational Physics, 57, pp. 327-360 (1985).

[11] *Ilyin V.P.* Incomplete factorisation methods for solving algebraic systems. Moscow, Nauka publishes, 1995 (in Russian).

[12] *Nikitin V.F., Smirnov N.N., Legros J.C.* Effect of fingering in porous media. 52-d IAF Congress. Toulouse, 2001, IAF-01-J.4.10.

[13] *Vedernikov A., Scheid B., Istasse E., Legros J.C.* Viscous fingering in miscible liquids under microgravity conditions. Physics of Fluids, 2001, Vol. 13, N9, p. S12.

[14] *Smirnov N.N., Nikitin V.F., Ivashnyov O.E., Legros J.C., Vedernikov A., Scheid B., Istasse E.* Instability in viscous fluids displacement from cracks and porous samples. Proc. 53-d IAF Congress, Houston, 2002, IAC-02-J.2.02., 11p.

[15] *Smirnov N.N., J. C. Legros, V. F. Nikitin, E. Istasse, L. Schramm, F. Wassmuth, and D'Arcy Hart.* Filtration in Artificial Porous Media and Natural Sands under Microgravity Conditions. Microgravity sci. technol. 2003, XIV/2, pp. 3-28.

[16] *Meiburg, E. & Homsy, G.M.* Nonlinear unstable viscous fingers in Hele-Show flows. II. Numerical simulation. Phys. Fluids 1988, 31(3).

[17] *Tanveer, S.* Surprises in viscous fingering. J. Fluid Mech.,2000, vol. 409, p.273.

[18] *Zhuravlev, P.* Zap Leningrad Com. Inst. 1956, 133, 54 (in Russian).

[19] *Saffman, P.G. & Taylor, G.J.* The penetration of a fluid into a porous medium of Hele-Show cell containing a more viscous fluid. Proc. R. Foc. Zond. 1958, A 245, 312.

[20] *Guan X., Pitchumani R.* Viscous fingering in a Hele-Shaw cell with finite viscosity ratio and interfacial tension. ASME Journal of Fluids Engineering, 2003. Vol. 125, No. 2, pp. 354-364.